Nanoscale

PAPER

View Article Online
View Journal | View Issue

Cite this: *Nanoscale*, 2021, **13**, 17465

Photochemical reduction of nanocrystalline maghemite to magnetite†

Hankyeol Jung [a] and Alina M. Schimpf *[a,b]

Received 9th May 2021,
Accepted 30th September 2021

DOI: 10.1039/d1nr02973h

rsc.li/nanoscale

We present a method for thephotochemical conversion of the inverse spinel iron oxides in which the mixed-valent magnetite phase (Fe_3O_4) is accessed from the maghemite phase (γ-Fe_2O_3) *via* a stable, colloidal nanocrystal-to-nanocrystal transformation. Anaerobic UV-irradiation of colloidal γ-Fe_2O_3 nanocrystals in the presence of ethanol as a sacrificial reductant yields reduction of some Fe^{3+} to Fe^{2+}, resulting in a topotactic reduction of γ-Fe_2O_3 to Fe_3O_4. This reduction is evidenced by the emergence of charge-transfer absorption and increased *d*-spacing in UV-irradiated nanocrystals. Redox titrations reveal that ~43% of Fe in <*d*> = 4.8 nm nanocrystals can be reduced with this method and comparison of optical data indicates similar reduction levels in <*d*> = 7.3 and 9.0 nm nanocrystals. Addition of excess acetaldehyde during photoreduction shows that the extent of reduction is likely pinned by the hydrogenation of acetaldehyde back to ethanol and can be increased with the use of an alkylborohydride sacrificial reductant. Photochemical reduction is accompanied by increased magnetization and emergence of magnetic features characteristic of Fe_3O_4. Overall, this work provides a reversible, post-synthetic strategy to obtain Fe_3O_4 nanocrystals with well-controlled Fe^{2+} compositions.

Superparamagnetic iron oxide nanocrystals, particularly magnetite (Fe_3O_4) and maghemite (γ-Fe_2O_3), have been extensively studied[1–5] due to their potential use in myriad technologies, including magnetoresistive devices,[6–13] biomedical diagnostics and treatments,[14–17] and water purification.[18–21] Phase-selective synthesis and use of these nanomaterials, however, are often challenging because Fe_3O_4 easily oxidizes to γ-Fe_2O_3 under ambient conditions, resulting in mixed phases and/or loss of the desired properties. For example, γ-Fe_2O_3 has a lower overall magnetic moment and decreased magnetocrystalline anisotropy compared to Fe_3O_4. Additionally, Fe_3O_4 can exhibit half-metallicity with a high degree of spin-polarization, while γ-Fe_2O_3 is electrically insulating. These properties make Fe_3O_4 more desirable for incorporation into spin transport devices. Furthermore, catalytic degradation of organic pollutants requires the oxidation of Fe^{2+},[19] not natively present in γ-Fe_2O_3. Here, we present a method to photochemically transform γ-Fe_2O_3 or Fe_3O_4/γ-Fe_2O_3 mixtures into Fe_3O_4, enabling reversible, post-synthetic switching between the two phases.

Both Fe_3O_4 and γ-Fe_2O_3 crystallize in an inverse spinel structure, B(AB)X_4. In the case of Fe_3O_4, 1/3 of Fe cations are in the +2 oxidation state (the "A" cations) and occupy primarily octahedral (O_h) sites, while 2/3 are in the +3 oxidation state and are distributed equally between O_h and tetrahedral (T_d) sites (the "B" cations). γ-Fe_2O_3 is often described as Fe^{2+}-deficient Fe_3O_4 ($Fe_{3-\delta}O_4$, $\delta = 1/3$) because the 16 O_h sites in the unit cell are replaced by 40/3 Fe^{3+} and 8/3 vacancies. The structural similarity of these phases enables easy topotaxial oxidation of Fe_3O_4 to γ-Fe_2O_3,[22–31] which occurs even faster in nanocrystals than in the bulk due to the relatively high surface area. Consequently, nanostructures of these iron oxides often contain a mixture of Fe_3O_4 and γ-Fe_2O_3.[2,22,30–38] Many studies have focused on evaluating the extent and/or mechanism of oxidation in Fe_3O_4/γ-Fe_2O_3 nanocrystals,[2,13,22,27,30,32–38] but direct reduction of γ-Fe_2O_3 has rarely been successfully employed as a strategy for accessing Fe_3O_4 nanocrystals.[39–41] For example, the addition of excess catechol-type ligands to γ-Fe_2O_3 leads to only partial reduction, likely occurring at the surface while maintaining an oxidized γ-Fe_2O_3 core.[39]

Photochemical reduction has been used to introduce band-like charge-carriers into various metal oxide nanocrystals, including ZnO,[42–45] TiO_2,[45,46] and In_2O_3,[42] using a mild sacrificial reductant, such as ethanol (EtOH, CH_3CH_2OH). In this process (eqn (1)), UV illumination excites an electron across the metal–oxide nanocrystal (NC) bandgap and the strong oxidizing power of the photogenerated valence-band hole (h^+_{VB}) leads to oxidation of EtOH to acetaldehyde (CH_3CHO), which is irreversible unless more reducing potentials are accessed. The overall reaction deposits conduction-band electrons (e^-_{CB}) and charge-compensating protons. Notably, when ZnO nanocrystals are doped with Fe^{3+}, UV irradiation leads to localized reduction to

[a]*Materials Science and Engineering Program, University of California, San Diego, La Jolla, CA 92093, USA*
[b]*Department of Chemistry and Biochemistry, University of California, San Diego, La Jolla, CA 92093, USA. E-mail: aschimpf@ucsd.edu*

†Electronic supplementary information (ESI) available. See DOI: 10.1039/d1nr02973h

Fe^{2+} prior to accumulation of delocalized electrons.[47,48] These results, along with the similarly high oxidizing power of the γ-Fe_2O_3 valence band suggest that photochemical reduction of Fe^{3+} in γ-Fe_2O_3 should be feasible. Indeed, UV irradiation of Fe_3O_4 nanomaterials has been exploited for the *in situ* reduction of surface Fe^{3+} for Fenton-like reactions,[49–53] used in the catalytic degradation of wastewater contaminants. Here, we show that photo-oxidation of EtOH can be used to access Fe_3O_4 nanocrystals from γ-Fe_2O_3 or Fe_3O_4/γ-Fe_2O_3 mixtures.

$$e^-_{CB}, h^+_{VB} : NC + CH_3CH_2OH \rightarrow 2e^-_{CB} : NC + 2H^+ + CH_3CHO \quad (1)$$

Results and analysis

Colloidal γ-Fe_2O_3 nanocrystals were synthesized *via* thermal decomposition of iron pentacarbonyl in a mixture of oleic acid and a dialkyl ether (R_2O; R = octyl or benzyl).[54] This synthesis yields nanocrystals with mixtures of Fe_3O_4 and γ-Fe_2O_3, likely in a core/shell architecture,[33] which were oxidized to γ-Fe_2O_3 by additional heating in air. The resulting γ-Fe_2O_3 nanocrystals were photoreduced following procedures used for other colloidal metal oxide nanocrystals.[42–46] Briefly, anaerobic solutions of the nanocrystals (~1 mM Fe) in toluene/THF (1/1) containing 124 EtOH/Fe as a sacrificial reductant were irradiated using a 365-nm LED (0.5 W cm^{-2}). The absorption was measured periodically and samples were considered to be maximally photoreduced when the absorption stopped changing over ~30 min. Fig. 1a shows the electronic absorption spectra (top) and differential absorption (bottom) of a solution of <*d*> = 4.8 nm nanocrystals with increasing exposure to UV irradiation (following the direction of the arrows). Prior to UV irradiation, the solution is yellow (Fig. 1a, inset, left) and shows absorption only above 2.0 eV, corresponding to the bandgap of maghemite derived from O(2*p*) → Fe(3*d*) transitions.[55] Following UV irradiation, the nanocrystal solution turns dark brown (Fig. 1a, inset, right) due to new near-IR and visible absorption. These new features are consistent with the intervalence charge transfer (IVCT) and intersublattice charge transfer (ISCT) absorption characteristic of Fe_3O_4.[55–57] Concomitant with a growth in near-IR/visible absorption, a decrease in the absorption above 3.0 eV is observed. This decrease in the O(2*p*) → Fe(3*d*) transition in consistent with a greater ratio of Fe^{2+}/Fe^{3+}, as is expected for the reduction of γ-Fe_2O_3 to Fe_3O_4. These spectroscopic changes mirror those observed when Fe_3O_4 nanocrystals are chemically oxidized to γ-Fe_2O_3.[24]

Changes in the iron oxide structure before and after photochemical reduction were also evaluated by powder X-ray diffraction. Fig. 1b shows a comparison of the (422), (511) and (440) reflections before (yellow) and after 3 h UV irradiation (brown). Full powder patterns (2θ = 10–80°) are provided in Fig. S1.† Following UV irradiation, all resolvable reflections

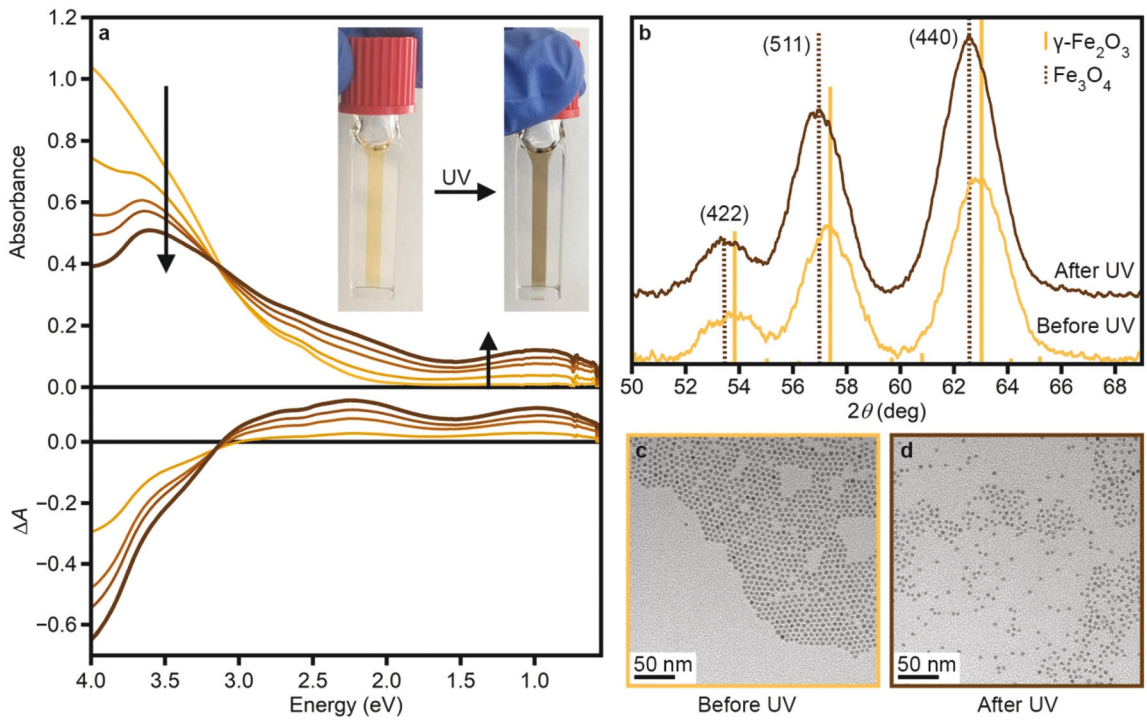

Fig. 1 Photochemical conversion of γ-Fe_2O_3 to Fe_3O_4 in <*d*> = 4.8 nm nanocrystals. (a) Absorption spectra of nanocrystals ([Fe] = 1.0 mM) with increasing UV irradiation. Inset: Photographs of the colloidal suspension before (left) and after (right) 3 h UV irradiation show a color change from yellow to brown. (b) Powder X-ray diffraction patterns before (yellow) and after (brown) 3 h UV irradiation. Simulated patterns for γ-Fe_2O_3 (solid yellow)[58] and Fe_3O_4 (dashed brown)[59] are shown for reference. All patterns are plotted for diffraction of Cu Kα radiation (1.5406 Å). Full powder patterns are provided in Fig. S1.† TEM images of nanocrystals (c) before and (d) after 3 h UV irradiation. Size-distributions are provided in Fig. S2.†

shift to lower values of 2θ (Table S1†), consistent with the larger unit cell of Fe_3O_4 compared to γ-Fe_2O_3 (Table S2†). Importantly, transmission electron microscopy (TEM) reveals no change in the size or size-distribution of the nanocrystals after UV irradiation (Fig. 1c, d and S2†). When the same method was used with <*d*> = 9.0 nm γ-Fe_2O_3 nanocrystals, absorption spectroscopy (Fig. S3a†) powder X-ray diffraction (Fig. S3b†) and Raman spectroscopy[4,60] (Fig. S4†) revealed analogous conversion to Fe_3O_4.

To determine the extent of reduction, photoreduced nanocrystals were titrated using methods similar to those developed for other photodoped metal oxide nanocrystals[42,44,45,61] and frameworks.[62] Specifically, the incremental addition of copper (II) triflate ($Cu(OTf)_2$) leads to a decrease in the absorption below 3.0 eV and a recovery of the bleach above 3.0 eV (Fig. 2). Spectra are plotted as the differential absorption and extinction ($\Delta A = A - A_{BeforeUV}$ and $\Delta\varepsilon = \varepsilon - \varepsilon_{BeforeUV}$, respectively). The integrated differntial intensity of the IVCT/ISCT absorption (0.8–3.0 eV) was plotted as a function of Cu^{2+}/Fe (Fig. 2, inset). Up to ~0.2 Cu^{2+}/Fe, the absorption decreases linearly with Cu^{2+} addition. Further addition of Cu^{2+} leads to very little change in the absorption spectra (Fig. S5†). Similar results are seen even with the use of a stronger oxidant (Ce^{4+}, Fig. S6†). These observations suggest that a subset of the Fe is more stably reduced to Fe^{2+} or is kinetically more difficult to reoxidize. This subset is comparable to the subset of Fe^{2+} in the as-synthesized nanocrystals (Fig. S7†), which are expected to contain a Fe_3O_4/γ-Fe_2O_3 core/shell structure.[54] Heating of the nanocrystal solutions containing 0.58 equiv. Cu^{2+}/Fe leads to further recovery of the initial spectroscopic features (Fig. S5†) but could not be performed for extended times without solvent evaporation. The ratio of Fe^{2+} was thus estimated by extrapolating the fit of the linear regime of the titration. A similar method was used for the titration of delocalized electrons in Sn^{4+}:In_2O_3 nanocrystals in which photodoped electrons could be removed with a mild oxidant but aliovalently introduced electrons could not.[42]

A total of four titrations were conducted and the linear regime (up to ~0.2 oxidant/Fe) was extrapolated to estimate the fraction of Fe that had been reduced. Results from each titration are provided in Table S3.† Based on these experiments, 43 ± 3% of Fe is in the +2 oxidation state following UV irradiation. This value is slightly greater than the fraction of Fe^{2+} in Fe_3O_4 (33%), suggesting that photochemical reduction can be used to completely convert from γ-Fe_2O_3 to Fe_3O_4.

To confirm that photochemical reduction can occur throughout the nanocrystals and not only at the surface, various-sized nanocrystals were evaluated. Fig. 3 shows the differential extinction spectra of maximally photoreduced nanocrystals with average diameters of <*d*> = 4.8 nm (dotted brown, reproduced from Fig. 2), <*d*> = 7.0 nm (solid pink) and <*d*> = 9.0 nm (dashed blue). If reduction was only happening at the surface, a systematic decrease in $\Delta\varepsilon$ would be expected for increasing nanocrystal size due to decreasing surface-area/volume. A lack of such trend suggests that the reduction can penetrate the volume of the nanocrystal for the sizes investigated here. It is worth noting that ensembles with larger average sizes were photoreduced more slowly (Fig. 3, inset; Table S4†), possibly due to slow charge-diffusion from the surface into the nanocrystal volume.

It has been shown previously that degenerate photodoping of ZnO nanocrystals with EtOH as the sacrificial reductant is pinned by the hydrogenation of acetaldehyde to EtOH, which is the reverse of the EtOH photooxidation reaction.[42] To test if this is also the limiting factor for iron oxide reduction, γ-Fe_2O_3 nanocrystals were photodoped in the presence of various amounts of added acetaldehyde (Fig. S8†). Here, the integrated differential extinction of the IVCT/ISCT region (0.8–3.0 eV) is used to rep-

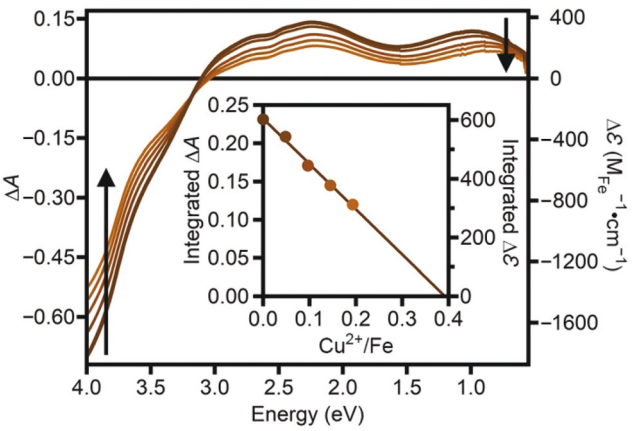

Fig. 2 Absorption and extinction (plotted as $\Delta A = A - A_{BeforeUV}$ and $\Delta\varepsilon = \varepsilon - \varepsilon_{BeforeUV}$, respectively) spectra of photodoped <*d*> = 4.8 nm nanocrystals ([Fe] = 1.0 mM) with added $Cu(OTf)_2$. Arrows show direction of increased addition of oxidant, from 0 to ~0.2 equiv. Cu^{2+}/Fe. Inset: Integrated (0.8–3.0 eV) ΔA and $\Delta\varepsilon$ as a function of Cu^{2+}/Fe. The linear fit is used to estimate the fraction of Fe^{2+} in the photodoped nanocrystals (39%).

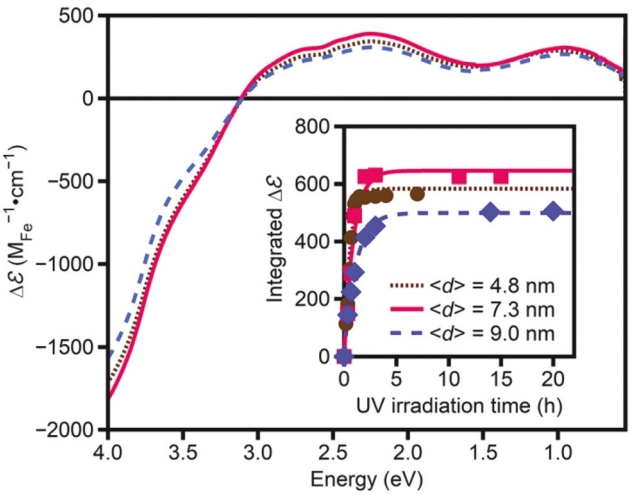

Fig. 3 Extinction spectra ($\Delta\varepsilon = \varepsilon - \varepsilon_{BeforeUV}$) of maximally photodoped <*d*> = 4.8 nm (brown circles), <*d*> = 7.3 nm (pink squares) and <*d*> = 9.0 nm (blue diamonds) nanocrystals. Inset: Integrated extinction as a function of time.

resent the level of photoreduction. Similar to the photodoping of ZnO nanocrystals, the maximum photoreduction decreases with added acetaldehyde, suggesting that acetaldehyde hydrogenation can limit the photoreduction of γ-Fe_2O_3.

It has also been shown in ZnO nanocrystals that the use of alkylborohydrides as sacrificial reductants leads to an increase in the maximum photodoping level.[44] In the case of γ-Fe_2O_3, addition of ~50 equiv. $LiEt_3BH$/Fe led to direct reduction of <*d*> = 4.8 nm nanocrystals, even without UV irradiation (Fig. S9i†). This level of reduction is comparable to the maximum level of photoreduction achieved using EtOH as the sacrificial reductant (Fig. S9ii†). UV irradiation of the $LiEt_3BH$-reduced sample leads to further spectroscopic changes (Fig. S9iii†), which are distinct from those observed with EtOH. Namely, the lowest energy transition (~1.0 eV) blue shifts, which was not observed for photochemical reduction with EtOH (Fig. 1a). Additionally, a large bleach of the absorbance above ~2.2 eV leads to the loss of the isosbestic point, normally observed at ~3.1 eV (Fig. 1a).[24] These changes make quantification of reduction by integrated intensity unreliable but may suggest reduction beyond the pure Fe_3O_4 phase. No new phase was observable by powder X-ray diffraction, however (Fig. S10†).

Finally, changes in the magnetic behavior upon photoreduction were monitored using superconducting quantum interference device (SQUID) magnetometry. For these measurements, anaerobic nanocrystal solutions (~50 mg, 10–20 mM) in toluene/THF/EtOH (75/75/1) were sealed in a quartz tube. Magnetic data were collected on the as-prepared sample ("Before UV") and after varying UV irradiation times (Fig. 4). Importantly, the magnetization *vs.* field (*M vs. H*, Fig. 4a) reveals a 51% increase in the saturation magnetization (M_s) following 6.5 h UV irradiation. This increase is consistent with phase-conversion to Fe_3O_4 in which the presence of Fe^{2+} contributes to higher magnetization due to ferromagnetic coupling with Fe^{3+} *via* double-exchange.[63,64] A similar, reverse trend has been observed upon the partial chemical oxidation of Fe_3O_4 to γ-Fe_2O_3.[65] Notably, there is negligible exchange bias (H_E) observed before and after UV irradiation (Table S5†), suggesting that reduction is distributed throughout the <*d*> = 4.8 nm nanocrystals.

The increase in magnetization is accompanied by (a) an opening of the hysteresis loop and an increase in the coercive field (H_c) from 14 to 1320 Oe (Fig. 4a) and (b) an increase in the blocking temperature (T_b), here defined as the maximum point of the zero-field-cooled (ZFC) curve in *M vs.* temperature (*T*) measurements, from 6 to 35 K (Fig. 4b). These increases are consistent with the larger intrinsic magnetocrystalline anisotropy of Fe_3O_4.[66,67] Further UV irradiation of the <*d*> = 4.8 nm nanocrystals leads to the emergence of a feature at ~120 K (Fig. 4b), consistent with the Verwey transition[68–70]. The emergence of a Verwey transition with photochemical reduction is notable, as previous studies have shown that this transition is generally suppressed for nanocrystals with <*d*> < 20 nm and completely disappears when <*d*> < 6 nm due to the high percentage of surface sites that can easily host defects.[71]

Similar trends in M_s, H_c and T_b are seen following UV irradiation of larger (<*d*> = 9.0 nm) nanocrystals (Fig. S11†).

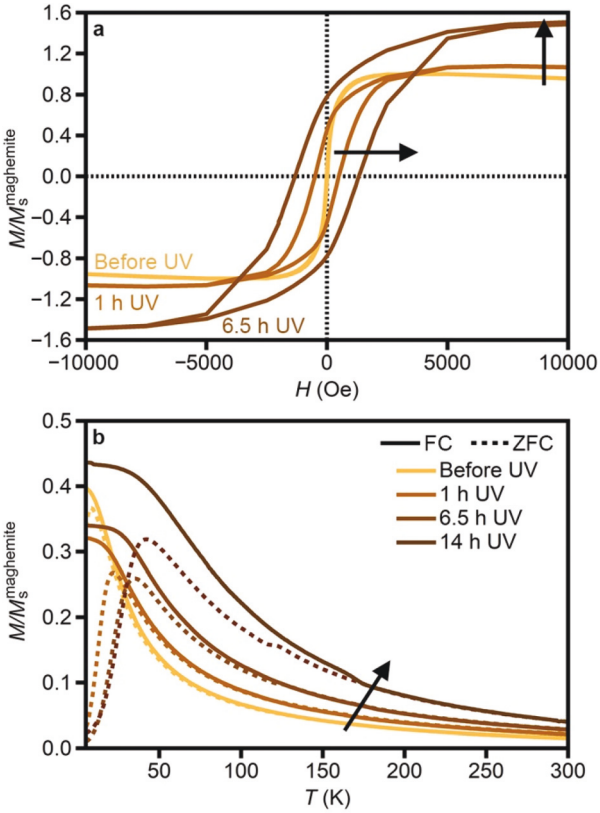

Fig. 4 Magnetic behavior of <*d*> = 4.8 nm nanocrystals before and after varying UV irradiation times. Magnetization as a function of (a) applied field at 5 K and (b) temperature for field-cooled (FC, solid lines, 100 Oe) and zero-field-cooled (ZFC, dashed lines) samples. All magnetization values (*M*) are given in terms of $M_s^{maghemite}$, which is the saturation magnetization at 5 K of the γ-Fe_2O_3 nanocrystals before UV irradiation. Arrows show changes with increasing UV irradiation.

These nanocrystals, however, display significant H_E following UV irradiation (Table S5†), which may suggest that photoreduction proceeds more heterogeneously in larger nanocrystals. The sharp magnetization feature at ~200 K in the most reduced nanocrystals (Fig. S11b) indicates the presence of a subpopulation of the further-reduced antiferromagnetic wüstite phase ($Fe_{1-x}O$; Neél temperature, T_N ~ 200 K).[72,73] The dominant superparamagnetic behavior (Fig. S11b†), however, suggests that that the fraction of $Fe_{1-x}O$ is small and $Fe_{1-x}O$ is not observed by powder X-ray diffraction (Fig. S12†).

Discussion

Based on the crystal structures of Fe_3O_4 and γ-Fe_2O_3, the reduction of Fe^{3+} in γ-Fe_2O_3 is expected to be favored at O_h A-sites. An idealized chemical equation for the photochemical reduction of γ-Fe_2O_3 ($(Fe_8^{III})_{tet}(Fe_{40/3}^{III})_{oct}O_{32}$), in which 50% of Fe_{oct}^{III} cations (all A cations) are reduced, is presented in Scheme 1a. The reduction of Fe_{oct}^{III} cations results in a charged nanocrystal in which charge-compensation is provided by H^+ generated from MeOH oxidation (Scheme 1a(i)). The reduced

a

$$\left(Fe_8^{III}\right)_{tet}\left(Fe_{40/3}^{III}\right)_{oct}O_{32}+\frac{10}{3}CH_3CH_2OH\rightarrow\left[\left(Fe_8^{III}\right)_{tet}\left(Fe_{20/3}^{III}Fe_{20/3}^{II}\right)_{oct}O_{32}\right]^{20/3-}+\frac{10}{3}CH_3CHO+\frac{20}{3}H^+ \quad \text{(i)}$$

$$\left[\left(Fe_8^{III}\right)_{tet}\left(Fe_{20/3}^{III}Fe_{20/3}^{II}\right)_{oct}O_{32}\right]^{20/3-}=\frac{8}{9}\left[\left\{\left(\mathbf{Fe_8^{III}}\right)_{\mathbf{tet}}\left(\mathbf{Fe_8^{III}Fe_8^{II}}\right)_{\mathbf{oct}}\mathbf{O_{32}}\right\}O_4\right]^{15/2-} \quad \text{(ii)}$$

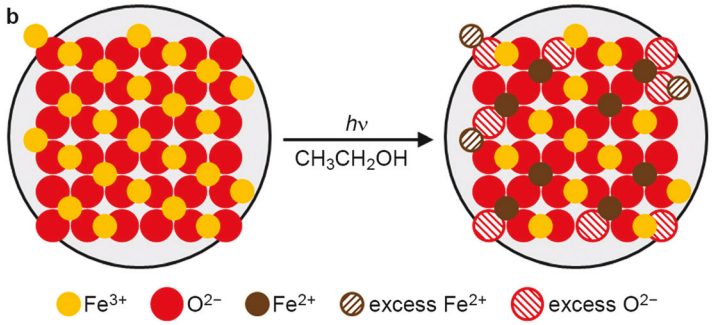

Scheme 1 (a) Idealized chemical equations for the photochemical reduction of γ-Fe_2O_3 with MeOH. (i) The reduction of 50% Fe_{oct}^{III} results in a charged nanocrystal, with charge-compensation provided by the H^+ generated from MeOH oxidation. (ii) The reduced nanocrystal can be rewritten in terms of a magnetite core with "excess" O atoms, which likely reside on the surface and are compensated by photogenerated H^+. (b) Abstract schematic depiction of the reduction of γ-Fe_2O_3 to Fe_3O_4, in which some ("excess") surface atoms are no longer part of the core nanocrystalline phase.

nanocrystal can be rewritten in terms of a magnetite core ($(Fe_8^{III})_{tet}(Fe_8^{III}Fe_8^{II})_{oct}O_{32}$) with "excess" O atoms (Scheme 1a(ii)), which likely reside on the surface and are compensated by the H^+ released during EtOH oxidation.

The nanocrystal reduction must first happen at surface Fe, after which charge-migration can lead to reduction of Fe in the bulk of the nanocrystal. The reduction of ~43% of Fe in the nanocrystals (Table S3†) is slightly higher than expected for a pure reduction of γ-Fe_2O_3 to Fe_3O_4, which should result in 33% of Fe being reduced. This excess Fe reduction, however, can occur at surface Fe (Scheme 1b, "excess Fe^{2+}"), and does not necessarily imply that B-site Fe ions are reduced in the bulk of the nanocrystal. Similarly, although γ-Fe_2O_3 and Fe_3O_4 have different Fe/O stoichiometries, the crystal structure can be relaxed at the surface, such that some of the O atoms are no longer counted in the core nanocrystal structure (Scheme 1a(ii); Scheme 1b, "excess O^{2-}"). Thus, as depicted in Scheme 1b, excess Fe-reduction and changes in Fe/O stoichiometry can be accounted for at the surface while the bulk of the reduced nanocrystal retains the stoichiometry of Fe_3O_4.

The "over-reduction" of Fe may also be responsible for the emergence of a small fraction of $Fe_{1-x}O$, which is detectable in larger nanocrystals *via* the appearance of a feature near T_N (Fig. S11b†). This phase could also be present in the smaller nanocrystals but masked due to the weakly superparamagnetic nature of small $Fe_{1-x}O$.[74] Importantly, nanocrystals are photochemically reduced to the same level, regardless of whether they start as fully oxidized (γ-Fe_2O_3) or as γ-Fe_2O_3/Fe_3O_4 mixtures (Fig. S13†). Photochemical reduction can thus be exploited to obtain a "normalized" Fe^{2+} content. The slower ensemble reduction with increasing nanocrystal size (Table S4†) suggests that this method is effective over a broad size range and only limited by charge-diffusion from the surface into the nanocrystal volume. This limit provides a facile strategy for post synthetic and reversible tuning of the exchange bias in single-component iron oxide nanostructures (Fig. 4, Table S5†).

The photochemical addition of delocalized electrons to ZnO nanocrystals has previously been shown to be pinned by aldehyde hydrogenation, which is negligible in as-prepared nanocrystals but becomes more favorable at increased electron densities.[42] The lower photochemical reduction of γ-Fe_2O_3 in the presence of added acetaldehyde (Fig. S8†) suggests that hydrogenation of acetaldehyde could also be limiting the photochemical reduction of γ-Fe_2O_3. Catalytic hydrogenation of aldehydes by iron oxides has been reported at slightly elevated temperatures (60 °C) but requires the use of a noble metal catalyst and an atmosphere of H_2.[75,76] In our case, aldehyde hydrogenation likely becomes favorable due to an increasingly negative Fermi level with increasing Fe^{2+} content. Indeed, pre-reduction of Fe_2O_3 has been shown to increase its activity in benzaldehyde hydrogenolysis.[77]

Summary and conclusions

We demonstrate a new strategy for controlling the oxidation state of Fe in inverse spinel iron oxide nanocrystals using photochemical reduction. Anaerobic UV-irradiation of colloidal γ-Fe_2O_3 nanocrystals results in new charge-transfer absorption, increased *d*-spacing and enhanced magnetization, characteristic of a topotactic reduction to Fe_3O_4. Redox titrations reveal that ~43% of Fe in $\langle d \rangle$ = 4.8 nm nanocrystals can be reduced with this method, indicating full conversion to Fe_3O_4, with excess reduction likely at the surface of the nanocrystals. As with other metal oxide nanocrystals, this photoreduction is likely pinned by the hydrogenation of acetaldehyde

back to EtOH and can be increased with the use of $LiEt_3BH$ as sacrificial reductant. Reduction in the presence of EtOH proceeds to the same level, regardless of starting point, providing a post-synthetic method for obtaining well-controlled Fe^{2+} concentrations across various samples. Overall, this strategy allows for facile access to the desired properties of fully reduced Fe_3O_4 colloidal nanocrystals.

Conflicts of interest

There are no conflicts to declare.

Acknowledgements

TEM data were collected at the UCSD Cellular and Molecular Medicine Electron Microscopy Facility (NIH 1S10OD023527) and the UCSD National Center for Microscopy and Imaging Research (NIH 1R24GM137200-01). Raman data were collected using instrumentation supported by the U. S. National Science Foundation through the UCSD Materials Research Science and Engineering Center (DMR-2011924). The authors thank Prof. J. D. Rinehart and B. H. Zhou for assistance with magnetic measurements and analysis.

References

1 S. Laurent, D. Forge, M. Port, A. Roch, C. Robic, L. V. Elst and R. N. Muller, Magnetic Iron Oxide Nanoparticles: Synthesis, Stabilization, Vectorization, Physicochemical Characterizations, and Biological Applications, *Chem. Rev.*, 2008, **108**, 2064.

2 A. Demortiere, P. Panissod, B. P. Pichon, G. Pourroy, D. Guillon, B. Donnio and S. Begin-Colin, Size-Dependent Properties of Magnetic Iron Oxide Nanocrystals, *Nanoscale*, 2011, **3**, 225.

3 J. Liu, Z. H. Wu, Q. Y. Tian, W. Wu and X. H. Xiao, Shape-Controlled Iron Oxide Nanocrystals: Synthesis, Magnetic Properties and Energy Conversion Applications, *CrystEngComm*, 2016, **18**, 6303.

4 M. Testa-Anta, M. A. Ramos-Docampo, M. Comesana-Hermo, B. Rivas-Murias and V. Salgueirino, Raman spectroscopy to unravel the magnetic properties of iron oxide nanocrystals for bio-related applications, *Nanoscale Adv.*, 2019, **1**, 2086.

5 A. V. Samrot, C. S. Sahithya, A.,J. Selvarani, S. K. Purayil and P. Ponnaiah, A Review on Synthesis, Characterization and Potential Biological Applications of Superparamagnetic Iron Oxide Nanoparticles, *Curr. Res. Green Sustain. Chem.*, 2021, **4**, 100042.

6 H. Zeng, C. T. Black, R. L. Sandstrom, P. M. Rice, C. B. Murray and S. H. Sun, Magnetotransport of Magnetite Nanoparticle Arrays, *Phys. Rev. B: Condens. Matter Mater. Phys.*, 2006, **73**, 020402(R).

7 J. Chen, X. C. Ye, S. J. Oh, J. M. Kikkawa, C. R. Kagan and C. B. Murray, Bistable Magnetoresistance Switching in Exchange-Coupled $CoFe_2O_4$–Fe_3O_4 Binary Nanocrystal Superlattices by Self-Assembly and Thermal Annealing, *ACS Nano*, 2013, **7**, 1478.

8 S. Kohiki, T. Kinoshita, K. Nara, K. Akiyama-Hasegawa and M. Mitome, Large, Negative Magnetoresistance in an Oleic Acid-Coated Fe_3O_4 Nanocrystal Self-Assembled Film, *ACS Appl. Mater. Interfaces*, 2013, **5**, 11584.

9 A. Mitra, B. Barick, J. Mohapatra, H. Sharma, S. S. Meena and M. Aslam, Large Tunneling Magnetoresistance in Octahedral Fe3O4 Nanoparticles, *AIP Adv.*, 2016, **6**, 055007.

10 C. P. Jiang, S. M. Ng, W. Leung and P. W. T. Pong, Magnetically Assembled Iron Oxide Nanoparticle Coatings and Their Integration With Pseudo-Spin-Valve Thin Films, *J. Mater. Chem. C*, 2017, **5**, 252.

11 Y. Lin, H. Y. Xu, Z. Q. Wang, T. Cong, W. Z. Liu, H. L. Ma and Y. C. Liu, Transferable and Flexible Resistive Switching Memory Devices Based on PMMA Films With Embedded Fe_3O_4 Nanoparticles, *Appl. Phys. Lett.*, 2017, **110**, 193503.

12 B. H. Zhou and J. D. Rinehart, Pseudo Spin Valve Behavior in Colloidally Prepared Nanoparticle Films, *ACS Appl. Electron. Mater.*, 2019, **1**, 1065.

13 H. H. Nguyen, H. K. T. Ta, S. Park, T. B. Phan and N. K. Pham, Resistive Switching Effect and Magnetic Properties of Iron Oxide Nanoparticles Embedded-Polyvinyl Alcohol Film, *RSC Adv.*, 2020, **10**, 12900.

14 K. M. Krishnan, Biomedical Nanomagnetics: A Spin Through Possibilities in Imaging, Diagnostics, and Therapy, *IEEE Trans. Magn.*, 2010, **46**, 2523.

15 R. A. Frimpong and J. Z. Hilt, Magnetic Nanoparticles in Biomedicine: Synthesis, Functionalization and Applications, *Nanomedicine*, 2010, **5**, 1401.

16 K. Yan, P. H. Li, H. E. Zhu, Y. J. Zhou, J. D. Ding, J. Shen, Z. Li, Z. S. Xu and P. K. Chu, Recent Advances in Multifunctional Magnetic Nanoparticles and Applications to Biomedical Diagnosis and Treatment, *RSC Adv.*, 2013, **3**, 10598.

17 N. Lee, D. Yoo, D. Ling, M. H. Cho, T. Hyeon and J. Cheon, Iron Oxide Based Nanoparticles for Multimodal Imaging and Magnetoresponsive Therapy, *Chem. Rev.*, 2015, **115**, 10637.

18 M. M. Khin, A. S. Nair, V. J. Babu, R. Murugan and S. Ramakrishna, A Review on Nanomaterials for Environmental Remediation, *Energy Environ. Sci.*, 2012, **5**, 8075.

19 P. V. Nidheesh, Heterogeneous Fenton Catalysts for the Abatement of Organic Pollutants From Aqueous Solution: a Review, *RSC Adv.*, 2015, **5**, 40552.

20 K. K. Kefeni, B. B. Mamba and T. A. M. Msagati, Application of Spinel Ferrite Nanoparticles in Water and Wastewater Treatment: A Review, *Sep. Purif. Technol.*, 2017, **188**, 399.

21 H. W. Luo, Y. F. Zeng, D. Q. He and X. L. Pan, Application of Iron-Based Materials in Heterogeneous Advanced Oxidation Processes for Wastewater Treatment: A Review, *Chem. Eng. J.*, 2021, **407**, 127191.

22 L. K. Bogart, C. Blanco-Andujar and Q. A. Pankhurst, Environmental Oxidative Aging of Iron Oxide Nanoparticles, *Appl. Phys. Lett.*, 2018, **113**, 133701.

23 P. S. Sidhu, R. J. Gilkes and A. M. Posner, Mechanism of the Low Temperature Oxidation of Synthetic Magnetites, *J. Inorg. Nucl. Chem.*, 1977, **39**, 1953.
24 J. Tang, M. Myers, K. A. Bosnick and L. E. Brus, Magnetite Fe_3O_4 Nanocrystals: Spectroscopic Observation of Aqueous Oxidation Kinetics, *J. Phys. Chem. B*, 2003, **107**, 7501.
25 S. P. Schwaminger, D. Bauer, P. Fraga-Garcia, F. E. Wagner and S. Berensmeier, Oxidation of Magnetite Nanoparticles: Impact on Surface and Crystal Properties, *CrystEngComm*, 2017, **19**, 246.
26 O. Ozdemir, D. J. Dunlop and B. M. Moskowitz, The Effect of Oxidation on the Verwey Transition in Magnetite, *Geophys. Res. Lett.*, 1993, **20**, 1671.
27 U. Colombo, G. Fagherazzi, F. Gazzarri, G. Lanzavecchia and G. Sironi, Mechanism of Low Temperature Oxidation of Magnetites, *Nature*, 1968, **219**, 1036.
28 K. J. Gallaghe, W. Feitknec and U. Mannweil, Mechanism of Oxidation of Magnetite to γ-Fe_2O_3, *Nature*, 1968, **217**, 1118.
29 A. G. Roca, J. F. Marco, M. D. Morales and C. J. Serna, Effect of Nature and Particle Size on Properties of Uniform Magnetite and Maghemite Nanoparticles, *J. Phys. Chem. C*, 2007, **111**, 18577.
30 T. J. Daou, G. Pourroy, S. Begin-Colin, J. M. Greneche, C. Ulhaq-Bouillet, P. Legare, P. Bernhardt, C. Leuvrey and G. Rogez, Hydrothermal Synthesis of Monodisperse Magnetite Nanoparticles, *Chem. Mater.*, 2006, **18**, 4399.
31 T. J. Daou, J. M. Greneche, G. Pourroy, S. Buathong, A. Derory, C. Ulhaq-Bouillet, B. Donnio, D. Guillon and S. Begin-Colin, Coupling Agent Effect on Magnetic Properties of Functionalized Magnetite-Based Nanoparticles, *Chem. Mater.*, 2008, **20**, 5869.
32 H. S. Dehsari, V. Ksenofontov, A. Moller, G. Jakob and K. Asadi, Determining Magnetite/Maghemite Composition and Core-Shell Nanostructure from Magnetization Curve for Iron Oxide Nanoparticles, *J. Phys. Chem. C*, 2018, **122**, 28292.
33 R. Frison, G. Cernuto, A. Cervellino, O. Zaharko, G. M. Colonna, A. Guagliardi and N. Masciocchi, Magnetite–Maghemite Nanoparticles in the 5–15 nm Range: Correlating the Core–Shell Composition and the Surface Structure to the Magnetic Properties. A Total Scattering Study, *Chem. Mater.*, 2013, **25**, 4820.
34 G. M. da Costa, C. Blanco-Andujar, E. De Grave and Q. A. Pankhurst, Magnetic Nanoparticles for in Vivo Use: A Critical Assessment of Their Composition, *J. Phys. Chem. B*, 2014, **118**, 11738.
35 C. A. Gorski and M. M. Scherer, Determination of Nanoparticulate Magnetite Stoichiometry by Mossbauer Spectroscopy, Acidic Dissolution, and Powder X-Ray Diffraction: A Critical Review, *Am. Mineral.*, 2010, **95**, 1017.
36 Y. Hwang, S. Angappane, J. Park, K. An, T. Hyeon and J. G. Park, Exchange Bias Behavior of Monodisperse Fe_3O_4/É£-Fe_2O_3 Core/Shell Nanoparticles, *Curr. Appl. Phys.*, 2012, **12**, 808.
37 C. Martinez-Boubeta, K. Simeonidis, M. Angelakeris, N. Pazos-Perez, M. Giersig, A. Delimitis, L. Nalbandian, V. Alexandrakis and D. Niarchos, Critical Radius for Exchange Bias in Naturally Oxidized Fe Nanoparticles, *Phys. Rev. B: Condens. Matter Mater. Phys.*, 2006, **74**, 054430.
38 J. S. Salazar, L. Perez, O. de Abril, T. P. Lai, D. Ihiawakrim, M. Vazquez, J. M. Greneche, S. Begin-Colin and G. Pourroy, Magnetic Iron Oxide Nanoparticles in 10–40 nm Range: Composition in Terms of Magnetite/Maghemite Ratio and Effect on the Magnetic Properties, *Chem. Mater.*, 2011, **23**, 1379.
39 P. Daniel, S. I. Shylin, H. Lu, M. N. Tahir, M. Panthofer, T. Weidner, A. Moller, V. Ksenofontova and W. Tremel, The Surface Chemistry of Iron Oxide Nanocrystals: Surface Reduction of γ-Fe_2O_3 to Fe_3O_4 by Redox-Active Catechol Surface Ligands, *J. Mater. Chem. C*, 2018, **6**, 326.
40 I. Martinez-Mera, C. Gutierrez-Wing, C. Arganis-Juarez and A. R. Vilchis-Nestor, Reduction of Maghemite to Magnetite Over 304SS, in the Presence of Silver Nanoparticles, *Surf. Coat. Technol.*, 2017, **324**, 338.
41 J. Azadmanjiri, G. P. Simon, K. Suzuki, C. Selomulya and J. D. Cashion, Phase Reduction of Coated Maghemite (γ-Fe_2O_3) Nanoparticles Under Microwave-Induced Plasma Heating for Rapid Heat Treatment, *J. Mater. Chem.*, 2012, **22**, 617.
42 G. M. Carroll, A. M. Schimpf, E. Y. Tsui and D. R. Gamelin, Redox Potentials of Colloidal n-Type ZnO Nanocrystals: Effects of Confinement, Electron Density, and Fermi-Level Pinning by Aldehyde Hydrogenation, *J. Am. Chem. Soc.*, 2015, **137**, 11163.
43 W. K. Liu, K. M. Whitaker, K. R. Kittilstved and D. R. Gamelin, Stable Photogenerated Carriers in Magnetic Semiconductor Nanocrystals, *J. Am. Chem. Soc.*, 2006, **128**, 3910.
44 A. M. Schimpf, C. E. Gunthardt, J. D. Rinehart, J. M. Mayer and D. R. Gamelin, Controlling Carrier Densities in Photochemically Reduced Colloidal ZnO Nanocrystals: Size Dependence and Role of the Hole Quencher, *J. Am. Chem. Soc.*, 2013, **135**, 16569.
45 J. N. Schrauben, R. Hayoun, C. N. Valdez, M. Braten, L. Fridley and J. M. Mayer, Titanium and Zinc Oxide Nanoparticles Are Proton-Coupled Electron Transfer Agents, *Science*, 2012, **336**, 1298.
46 H. H. Mohamed, C. B. Mendive, R. Dillert and D. W. Bahnemann, Kinetic and Mechanistic Investigations of Multielectron Transfer Reactions Induced by Stored Electrons in TiO_2 Nanoparticles: A Stopped Flow Study, *J. Phys. Chem. A*, 2011, **115**, 2139.
47 D. M. Zhou and K. R. Kittilstved, Electron Trapping on Fe^{3+} Sites in Photodoped ZnO Colloidal Nanocrystals, *Chem. Commun.*, 2016, **52**, 9101.
48 C. K. Brozek, D. M. Zhou, H. B. Liu, X. S. Li, K. R. Kittilstved and D. R. Gamelin, Soluble Supercapacitors: Large and Reversible Charge Storage in Colloidal Iron-Doped ZnO Nanocrystals, *Nano Lett.*, 2018, **18**, 3297.

49 M. Minella, G. Marchetti, E. De Laurentiis, M. Malandrino, V. Maurino, C. Minero, D. Vione and K. Hanna, Photo-Fenton Oxidation of Phenol With Magnetite as Iron Source, *Appl. Catal., B*, 2014, **154**, 102.
50 P. Avetta, A. Pensato, M. Minella, M. Malandrino, V. Maurino, C. Minero, K. Hanna and D. Vione, Activation of Persulfate by Irradiated Magnetite: Implications for the Degradation of Phenol under Heterogeneous Photo-Fenton-Like Conditions, *Environ. Sci. Technol.*, 2015, **49**, 1043.
51 N. P. F. Goncalves, M. Minella, D. Fabbri, P. Calza, C. Malitesta, E. Mazzotta and A. B. Prevot, Humic Acid Coated Magnetic Particles as Highly Efficient Heterogeneous Photo-Fenton Materials for Wastewater Treatments, *Chem. Eng. J.*, 2020, **390**, 124619.
52 J. F. Wu, J. Bai, Z. D. Wang, Z. W. Liu, Y. L. Mao, B. Liu and X. F. Zhu, UV-Assisted Nitrogen-Doped Reduced Graphene Oxide/Fe3O4 Composite Activated Peroxodisulfate Degradation of Norfloxacin, *Environ. Technol.*, 2020, DOI: 10.1080/09593330.2020.1779353.
53 N. P. F. Goncalves, M. Minella, G. Mailhot, M. Brigante and A. B. Prevot, Photo-Activation of Persulfate and Hydrogen Peroxide by Humic Acid Coated Magnetic Particles for Bisphenol A Degradation, *Catal. Today*, 2021, **361**, 43.
54 T. Hyeon, S. S. Lee, J. Park, Y. Chung and H. Bin Na, Synthesis, of Highly Crystalline and Monodisperse Maghemite Nanocrystallites Without a Size-Selection Process, *J. Am. Chem. Soc.*, 2001, **123**, 12798.
55 R. G. J. Strens and B. J. Wood, Diffuse Reflectance Spectra and Optical-Properties of Some Iron and Titanium-Oxides and Oxyhydroxides, *Mineral. Mag.*, 1979, **43**, 347.
56 S. K. Park, T. Ishikawa and Y. Tokura, Charge-Gap Formation Upon the Verwey Transition in Fe_3O_4, *Phys. Rev. B: Condens. Matter Mater. Phys.*, 1998, **58**, 3717.
57 W. F. J. Fontijn, P. J. van der Zaag, L. F. Feiner, R. Metselaar and M. A. C. Devillers, A Consistent Interpretation of the Magneto-Optical Spectra of Spinel Type Ferrites (Invited), *J. Appl. Phys.*, 1999, **85**, 5100.
58 E. Solano, C. Frontera, T. Puig, X. Obradors, S. Ricart and J. Ros, Neutron and X-Ray Diffraction Study of Ferrite Nanocrystals Obtained by Microwave-Assisted Growth. A Structural Comparison With the Thermal Synthetic Route, *J. Appl. Crystallogr.*, 2014, **47**, 414.
59 M. Fleet, The Structure of Magnetite, *Acta Crystallogr., Sect. B: Struct. Crystallogr. Cryst. Chem.*, 1981, **37**, 917.
60 M. I. Dar and S. A. Shivashankar, Single crystalline magnetite, maghemite, and hematite nanoparticles with rich coercivity, *RSC Adv.*, 2014, **4**, 4105.
61 A. M. Schimpf, S. T. Ochsenbein, R. Buonsanti, D. J. Milliron and D. R. Gamelin, Comparison of Extra Electrons in Colloidal N-Type Al^{3+}-Doped and Photochemically Reduced ZnO Nanocrystals, *Chem. Commun.*, 2012, **48**, 9352.
62 M. J. Turo, L. F. Chen, C. E. Moore and A. M. Schimpf, Co_2^{+}-Linked $[NaP_5W_{30}O_{110}]^{14-}$: A Redox-Active Metal Oxide Framework with High Electron Density, *J. Am. Chem. Soc.*, 2019, **141**, 4553.
63 A. Rosencwaig, Double Exchange and Metal–Nonmetal Transition in Magnetite, *Phys. Rev.*, 1969, **181**, 946.
64 R. J. McQueeney, M. Yethiraj, S. Chang, W. Montfrooij, T. G. Perring, J. M. Honig and P. Metcalf, Zener Double Exchange From Local Valence Fluctuations in Magnetite, *Phys. Rev. Lett.*, 2007, **99**, 246401.
65 R. L. Rebodos and P. J. Vikesland, Effects of Oxidation on the Magnetization of Nanoparticulate Magnetite, *Langmuir*, 2010, **26**, 16745.
66 J. M. D. Coey, *Magnetism and Magnetic Materials*, Cambridge University Press, Cambridge, 2010, p. xii.
67 P. Kucheryavy, J. B. He, V. T. John, P. Maharjan, L. Spinu, G. Z. Goloverda and V. L. Kolesnichenko, Superparamagnetic Iron Oxide Nanoparticles with Variable Size and an Iron Oxidation State as Prospective Imaging Agents, *Langmuir*, 2013, **29**, 710.
68 E. J. W. Verwey, Electronic Conduction of Magnetite (Fe_3O_4) and Its Transition Point at Low Temperatures, *Nature*, 1939, **144**, 327.
69 F. Walz, The Verwey Transition—a Topical Review, *J. Phys. Condens. Mater.*, 2002, **14**, R285.
70 M. Bohra, N. Agarwal and V. Singh, A Short Review on Verwey Transition in Nanostructured Fe_3O_4 Materials, *J. Nanomater.*, 2019, **2019**, 8457383.
71 J. Lee, S. G. Kwon, J. G. Park and T. Hyeon, Size Dependence of Metal–Insulator Transition in Stoichiometric Fe_3O_4 Nanocrystals, *Nano Lett.*, 2015, **15**, 4337.
72 M. S. Seehra and G. Srinivasan, Magnetic Studies of Nonstoichiometric Fe_zO and Evidence for Magnetic Defect Clusters, *J. Phys. C: Solid State Phys.*, 1984, **17**, 883.
73 C. A. Mccammon, Magnetic-Properties of Fe_xO (x>0.95) - Variation of Neel Temperature, *J. Magn. Magn. Mater.*, 1992, **104**, 1937.
74 M. Estrader, A. López-Ortega, I. V. Golosovsky, S. Estradé, A. G. Roca, G. Salazar-Alvarez, L. López-Conesa, D. Tobia, E. Winkler, J. D. Ardisson, W. A. A. Macedo, A. Morphis, M. Vasilakaki, K. N. Trohidou, A. Gukasov, I. Mirebeau, O. L. Makarova, R. D. Zysler, F. Peiró, M. D. Baró, L. Bergström and J. Nogués, Origin of the Large Dispersion of Magnetic Properties in Nanostructured Oxides: Fe_xO/Fe_3O_4 Nanoparticles as a Case Study, *Nanoscale*, 2015, **7**, 3002.
75 C. Milone, M. L. Tropeano, G. Gulino, G. Neri, R. Ingoglia and S. Galvagno, Selective Liquid Phase Hydrogenation of Citral on Au/Fe_2O_3 Catalysts, *Chem. Commun.*, 2002, 868.
76 C. Milone, C. Crisafulli, R. Ingoglia, L. Schipilliti and S. Galvagno, A Comparative Study on the Selective Hydrogenation of α, β Unsaturated Aldehyde and Ketone to Unsaturated Alcohols on Au Supported Catalysts, *Catal. Today*, 2007, **122**, 341.
77 D. Haffad, U. Kameswari, M. M. Bettahar, A. Chambellan and J. C. Lavalley, Reduction of Benzaldehyde on Metal Oxides, *J. Catal.*, 1997, **172**, 85.

